A case study on the far-field properties of propagating tropospheric gravity waves

Claudia Stephan *

Department of Atmospheric and Oceanic Sciences, University of Colorado, Boulder, Colorad o

M. Joan Alexander

NorthWest Research Associates, Inc., CoRA Office, Boulder, Colorado

Michael Hedlin, Catherine D. de Groot-Hedlin

Laboratory for Atmospheric Acoustics, U.C., San Diego, California

Lars Hoffmann

Jülich Supercomputing Centre, Forschungszentrum Jülich, Jülich, Germany

* *Current affiliation:* National Centre for Atmospheric Science - Climate, Department of Meteorology, University of Reading, Reading, United Kingdom

Corresponding author address: Claudia Stephan, Department of Meteorology, University of Reading, P.O. Box 243, Reading RG6 6BB, United Kingdom

E-mail: c.c.stephan@reading.ac.uk

ABSTRACT

Mesoscale gravity waves were observed by barometers deployed as part of the USArray Transportable Array on June 29, 2011 near two mesoscale convective systems in the Great Plains region of the US. Simultaneously, AIRS satellite data indicated stratospheric gravity waves propagating away from the location of active convection. Peak perturbation pressure values associated with waves propagating outside of regions where there was precipitation reached amplitudes close to 400 Pa at the surface. Here we investigate the origins of the waves and their relationship to observed precipitation with a specialized model study. Simulations with a 4-km resolution dry numerical model reproduce the propagation characteristics and amplitudes of the observed waves with a high degree of quantitative similarity despite the absence of any boundary layer processes, surface topography, or moist physics in the model. The model is forced with a three-dimensional, time-dependent latent heating/cooling field that mimics the latent heating inside the precipitation systems. The heating is derived from the network of weather radar precipitation observations. This shows that deep, intense latent heat release within the precipitation systems is the key forcing mechanism for the waves observed at ground level by the USArray. Furthermore, the model simulations allow for a more detailed investigation of the vertical structure and propagation characteristics of the waves. It is found that the stratospheric and tropospheric waves are triggered by the same sources, but have different spectral properties. Results also suggest that the propagating tropospheric waves may potentially remotely interact with and enhance active precipitation.

1. Introduction

The Earthscope USArray Transportable Array (TA) is a network of approximately 400 seismo-acoustic stations deployed on a 70-km Cartesian grid covering an area of 2,000,000 km^2 in the continental United States (Busby et al. 2006). The network moved eastward through station redeployments between 2004-2013, has since left the lower 48 states and is being redeployed in Alaska. Although the array was originally designed for seismological studies, in 2009 an atmospheric sensor package was deployed at TA sites along with the seismic sensors, recording pressure variations at the Earth's surface. Fig. 1 shows the locations of operating stations equipped with these sensors for the years 2010-2013.

Propagating signals in surface pressure surrounding severe precipitation systems have been observed with the TA, and were previously analyzed with a coherent detection method described by De Groot-Hedlin et al. (2014). Such large-amplitude surface pressure changes have previously been reported and connected to gravity waves, e.g. Koppel et al. (2000). The large number of TA sensors placed on a nearly regular Cartesian grid across a large region allows tracking of coherent signal propagation over long distances, and their method was designed to minimize spatial aliasing problems. The results showed that the typical 70-km spacing of the stations in the array permits the study of coherent signals with periods longer than $\sim$40 min and wavelengths longer than $\sim$40 km. These include a broad range of gravity waves with a wide range of propagation speeds. De Groot-Hedlin et al. (2014) showed that the largest amplitude waves also had the longest periods, and their analysis focused on signals in the 2-4 h band that displayed wavelengths longer than the inter-station spacing.

Here we investigate the apparent relationship of the gravity wave surface pressure signals observed at ground level by the TA to severe precipitation systems. We use precipitation measurements from Next-Generation Radar (NEXRAD) weather radar stations and a specialized model, which has previously been shown to accurately simulate gravity waves in the far-field emanating from severe precipitation systems over the continental US. We will consider a broader band of 1-8 h that includes most gravity waves that are well-resolved by the array.

Our study is an investigation into the origins of the observed waves, their propagation and vertical structure, and their relationship to precipitation in a detailed case-study. The selected case occurred during the night of June 28-29, 2011 over the central US when the TA spanned 90-100 °W longitudes over the Great Plains west of the Mississippi. The case, illustrated by radar mosaics in Fig. 2, includes two intense but relatively isolated precipitation systems: One over the northeastern corner of Texas on the evening of June 28th and a second over the Oklahoma Panhandle that intensified in the post-midnight hours of June 29th. These two precipitation systems occurred near the eastern and western edges of the TA, respectively, and the relatively isolated nature of the two precipitation systems makes this a good case for investigating the origins and remote propagation of gravity waves observed in TA surface pressure measurements.

We use the modeling approach of Stephan and Alexander (2015) to simulate gravity waves forced by realistically varying convective latent heating and cooling in an idealized dry version of the Weather Research and Forecasting (WRF) model (Skamarock et al. 2008). The heating/cooling field is three-dimensional and time-varying and derived directly from the NEXRAD-observed precipitation using an algorithm described in Stephan and Alexander (2015). The algorithm was trained on realistic simulations of severe precipitation systems with full-physics WRF hindcasts, but the use of the idealized model with radar precipitation in the present study permits direct comparisons to the spatial and temporal variations observed within the TA. Such direct comparisons are not possible in full-physics WRF hindcasts because the locations and timing of individual rain cells are never simulated accurately, yet these details are crucial for accurate simulation of the gravity wave responses.

With this method, we will investigate the horizontal and vertical propagation characteristics of the gravity wave field, the wave amplitudes and relationship to precipitation. Previous studies have suggested a potential role for convectively-generated gravity waves in the organization of convective rain clouds (e.g. Mapes (1993); Yang and Houze (1995); Tulich et al. (2007)). The importance of gravity waves in triggering and interacting with new convective systems has previously been demonstrated in two-dimensional models (Tulich and Mapes 2008; Lane and Zhang 2011; Stechmann and Majda 2009) and studies of observed events (Ruppert and Bosart 2014; Koch and Siedlarz 1999). It has been suggested that gravity waves may initiate new convective cells in the far field (e.g. Shige and Satomura (2001); Fovell (2002)).

While our dry model approach cannot directly investigate these feedbacks of gravity waves on precipitation, the model makes the normally invisible far-field gravity waves visible, permitting us to examine the realistically simulated gravity wave dynamics and their potential to influence low-level moisture convergence and precipitation. Our main goal, however, is to show that the new modeling approach can identify the sources of the waves observed by the high-density array of surface stations.

The paper is structured as follows: A summary of the weather situation during the time of this case study will be given in Section 2.*a*. Method and numerical model will be described in Section 2.*b*. We next examine the vertical structure of the simulated waves in Section 2.*c* and use linear theory to relate the shape of the heating profiles to the propagation characteristics of the waves. In Section 3 we compare the wave patterns and amplitudes of simulated and observed waves to show that the model predicts the surface measurements with good accuracy outside of precipitating regions. We further show that satellite observations of waves in the stratosphere above the precipitation systems are consistent with both the model predictions and observations at ground level. Section 4 examines the potential for the far-field gravity wave response associated with these convective regions to intensify remote convection. Section 5 is a summary and conclusion.

2. Numerical simulations

a. Weather conditions

During the time period of this case study, June 28-29, 2011, the large-scale synoptic pattern over North America at 500 hPa was dominated by a broad ridge centered over New Mexico/Texas that extended from the west coast to Florida. This high-pressure system caused record-breaking high temperatures in the southern US. At 12:00 UTC on June 28 a cold front extended from southeastern New Mexico to Tennessee. A series of severe precipitation systems developed along this front and moved southeastward over the course of the following 12 hours. The precipitation system in Fig. 2 over South-East Oklahoma was a remnant of these precipitation systems. After 01:00 UTC this system decayed. By 23:30 UTC on June 28 the cold front had turned into a stationary front that extended from the Oklahoma Panhandle along the Texas-Oklahoma boarder into northern Arkansas. This front separated hot air with surface temperatures exceeding 37°C in Texas from relatively cooler air to the north with surface temperatures of about 30°C, and a new precipitation system was developing on the southern side of the front. The precipitation system was located on the western end of the Oklahoma Panhandle and extended into Colorado and New Mexico. The front propagated northward and by 14:00 UTC on June 29 was located north of Oklahoma. Meanwhile the Panhandle precipitation system formed into a well organized squall line, which is clearly visible at 01:00 UTC in Fig. 2, and it moved eastward into Central Oklahoma (see Fig. 2 at 7:30 UTC). After 08:00 UTC this precipitation system started to decay as well.

b. Model and method

This study uses the modeling approach described in Stephan and Alexander (2015), where a nonlinear idealized dry version of the WRF model is forced with 4-km resolution latent heating/cooling derived from NEXRAD precipitation observations. The model does not include moist processes, a boundary layer, nor topography, i.e. there are no physics schemes active that represent boundary layer fluxes or radiation. A vertical heating/cooling profile is assigned to each grid point where the local precipitation rate exceeds 1 mm/10 min and is updated every 10 min. See Stephan and Alexander (2015) for details on the algorithm for generating the heating profiles. For several case studies it was shown that this model produces an excellent quantitative comparison to waves in the stratosphere that were observed by satellite. However, until now the realism of the simulated waves in the troposphere has not been validated.

Fig. 3 shows the 2000 km $\times$ 2000 km model domain in gold and the locations of individual NEXRAD radar stations that are used to derive a 4 km $\times$ 4 km 10 min mosaic of precipitation. The horizontal model domain is specified to have open boundary conditions. We obtain the Storm Total Rainfall Accumulation Product (STP, OFCM (2006)) for individual NEXRAD stations, which provides radar-estimated rainfall accumulations within 230 km of the radar in polar coordinates with a resolution of 2 km $\times$ 1°. Data from the individual stations are then interpolated in space and time to obtain Cartesian gridded maps.

The model run is initialized at 20:00 UTC on 28 June 2011 with one-dimensional horizontal-wind and potential temperature profiles, shown in Fig. 4. These are derived by averaging reanalyzed winds and temperatures from the Modern-Era Retrospective analysis for Research and Applications (MERRA, Rienecker et al. (2011)) over 24 h in the region within the dashed rectangle shown in Fig. 3. This area marks the region of strongest storm activity during the simulated period 20:00 UTC on 28 June, 2011 to 20:00 UTC on 29 June, 2011. The model includes 99 evenly spaced vertical levels extending from the surface to 24 km (30 hPa) with the upper 5 km consisting of a damping layer that was previously shown to prevent unphysical wave reflection at the upper boundary (Stephan and Alexander 2014).

Fig. 5 shows simulated pressure perturbations at 500 m above the surface at 2, 6 and 10 UTC. Red colors mark rain cells that exceed the convective threshold of 1 mm/10 min, i.e. regions where the heating field in the idealized model is nonzero. At 02:00 UTC both of the precipitation centers in the left panel of Fig. 2 are visible.

Different physical processes at different spatial scales are occurring simultaneously in the simulation. Recall that the model is initialized with a horizontally uniform profile of winds and potential temperature. In all three panels we observe that the slower timescale components of the diabatic convective heating input to the model modify the thermal structure and larger scale wind environment within the domain through potential vorticity changes. In the 2 UTC panel the signature of this modification is characterized by mostly positive pressure perturbations in the NW corner of the domain and mostly negative pressure perturbations in the SE corner of the domain. The initially horizontally-uniform background develops into a more complex state that resembles the actual environment surrounding deep convection. This adjustment to more realistic conditions is one reason why the modeling approach is successful in capturing the observed waves. The three panels of Fig. 5 show that waves are propagating both east- and westward. At any given time and location the local conditions, which are a combination of the initialization profile, mesoscale adjustments and wave interference, make certain directions more preferable.

The precipitation system centered at $\sim 95°$W is triggering strong westward propagating pressure waves with peak to peak amplitudes on the order of 300 Pa. A negative perturbation pressure wave is followed by a more slowly moving positive wave. The positive perturbation pressure wave reaches the other precipitation system located at $\sim 100°$W around 05:30 UTC. This second precipitation system is also triggering waves, which are clearly visible at the surface at 10:00 UTC.

From these maps and Fig. 2 it is apparent that most of the precipitation, and therefore waves, in the model domain and the surrounding region of the US are associated with the two well-confined precipitation systems. However, at 02:00 UTC and 10:00 UTC some isolated cells exist in the southeast corner of the model domain (Fig. 5). While these wave-generating cells are included in the model, other cells that lie outside of the model domain are not. When comparing to observations in Section 3 it should be taken into account that waves can propagate long distances and that some of the wave signals in the observations may be attributed to sources that lie outside of the simulated area.

c. Wave vertical structure and propagation characteristics

As mentioned in Section 1, the TA is a very useful observational network for studying the occurrence frequencies and horizontal propagation characteristics of gravity waves at the surface. The WRF simulation in addition is able to reveal the vertical structure of these waves, which is required for explaining their propagation characteristics and for assessing the impact such waves may have on the atmosphere hundreds of kilometers away from their origin.

Fig. 6 is a zonal cross section at 34°N and 00:40 UTC showing the vertical structure of small-scale propagating waves to the west of an active center of convection. The line to the left of each panel shows the shape of the mean heating/cooling profile inside the convective region as derived by the heating algorithm from observed precipitation, and the thin black line marks a value of zero. From the top panel of Fig. 6, which shows vertical velocity, we observe that the dominant vertical wavelength of the waves in the troposphere corresponds to twice the depth of the heating. Also evident are waves propagating into the stratosphere with shorter vertical scales. For hydrostatic and non-rotational gravity waves, the group velocity vector is along lines of constant phase and the ratio of the intrinsic vertical group velocity to the horizontal group velocity can be expressed as

$$|\hat{c}_{gz}/\hat{c}_{gh}| = |k_h/m| = |k_h \frac{\hat{c}_h}{N_{BV}}| = |\frac{\hat{\omega}}{N_{BV}}|, \tag{1}$$

where k_h is the horizontal wave number, $\hat{c}_h$ the intrinsic horizontal phase speed, m the vertical wave number and $\hat{\omega}$ the intrinsic frequency (Fritts and Alexander 2003). Since this quantity is inversely proportional to the buoyancy frequency N_{BV}, which in the stratosphere has approximately double its tropospheric value, waves get refracted to shorter vertical wavelength as they cross the tropopause, as evident in Fig. 6.

The bottom panel of Fig. 6 shows the corresponding perturbation pressure. Note that the anomalies are all positive because of the focus here on a small region that lies within the positive phase of the larger scale wave described in Fig. 5. Amplitudes are largest at the surface and decay linearly with altitude. In reality the Earth's surface in the area of interest is not flat but its elevation varies between 0.0-1.2 km above sea level. Given that the large-scale variations in pressure are on the order of several hundred Pa (see Fig. 5) we will neglect topography when comparing to the surface observations in Section 3, and focus on the model level at 500 m.

The vertical structure of the vertical velocity field displays some complexity. From linear theory it is expected that several wave modes are generated by the typical heating profiles in the model. It has been demonstrated that linear theory is successful in predicting the general shape of gravity wave spectra generated by a diabatic source in numerical simulations (Pandya and Alexander 1999; Song et al. 2003). Fig. 7 shows the decomposition of a heating profile $H(z)$ associated with a strong rain rate (thick black line in the right panel) into its first 10 (left panel) and first 3 (middle panel) Fourier components. The decomposition is given by

$$H(z) = \Sigma_{n=1}^{n=N} A_n \sin \frac{\pi n z}{D}. \tag{2}$$

Here, $D \approx 11$ km denotes the depth of the heating, which we define as the vertical distance between the bottom of the cooling layer and the top of the heating region. The Fourier decomposition consists of sine modes which meet the boundary conditions of vanishing amplitudes at the top and bottom of the vertical profile. This same analysis technique has previously been used in Alexander and Holton (2004) for interpreting far-field wave properties. The heating profile $H(z)$ is computed for a rain rate of 14 mm/10 min, which corresponds to the 99th percentile of 4 km $\times$ 4 km 10-min rain rates seen this study. The colored lines in Fig. 7 are the respective sums of the individual modes and are also shown in the right panel for comparison with the original profile.

As has been shown in Nicholls et al. (1991), linear theory predicts that the horizontal phase speed for a pure sine mode is given by

$$c_h = \frac{D}{n}\frac{N_{BV}}{\pi}. \tag{3}$$

The mean buoyancy frequency $N_{BV} = 0.012\ \mathrm{s}^{-1}$ in the heating/cooling region is computed from the initialization profile of dry potential temperature shown in Fig. 4.

Table 1 shows the theoretical phase speed and explained variance for the first ten Fourier modes. In deriving a vertical heating/cooling profile from rain rates, all parameters of the profile $H(z)$ (bottom/top of the heating/cooling layers, heating/cooling amplitudes and the levels at which these extrema are met) are linear functions of the rain rate. Therefore, choosing a different rain rate for computing $H(z)$ will make a difference to the phase speeds and the contribution of individual modes. However, for a 50% smaller rain rate phase speeds remain within 5% of those shown in Table 1. Therefore, a comparison between the single theoretical spectrum of Table 1 and the simulated spectrum can be made.

Fig. 8 shows normalized absolute momentum flux spectra, given by

$$F(\kappa, \omega) = \sqrt{(uw^*)^2 + (vw^*)^2} \tag{4}$$

at 3 km (left panel) and 17 km (right panel) as a function of wavenumber and frequency. These spectra are computed from perturbation wind velocities using a three-dimensional Fourier analysis. Details of the computation are described in Stephan and Alexander (2014). Lines of constant phase speed labeled in units of m/s are shown in white. Prominent lobes appear near the predicted top four ($n = 1, 2, 3, 4$) mode speeds of 40, 20, 15 and 10 m/s. The $n = 1$ mode is more pronounced in the stratosphere at 17 km compared to the 3 km level and the slowest $n > 5$ modes are more prominent in the troposphere. Eq. (1) predicts that for a given horizontal wavenumber k_h waves with larger horizontal phase speeds $\hat{c}_h$ escape into the stratosphere more quickly. This is consistent with the relatively larger abundance of slow (fast) waves in the troposphere (stratosphere). Deviations from the theoretical spectrum are expected for two reasons. As mentioned above, we assumed one specific rain rate for calculating the numbers in Table 1. Given that a wide variety of rain rates exist in the

24-h simulation, the simulated spectrum becomes blurred and continuous in wavenumber-frequency space. Secondly, the Fourier analysis is based on 24 hours. This is enough time for waves, especially the fast waves of the $n = 1$ mode, to leave the domain and explains why the $n = 1$ mode is not as prominent in Fig. 8 as one might expect from its contribution (Table 1).

3. Comparisons with observations

This study uses data from barometric pressure sensors in the atmospheric sensor package deployed at each site of the TA. These instruments measure ambient pressure with an accuracy of 0.2 Pa, with the data digitized at 1 Hz. For further details see De Groot-Hedlin et al. (2014).

Fig. 9 shows model perturbation pressure in units of Pa sampled at locations of TA installations and the corresponding TA recorded observations at 2-h intervals. A 1-8 h bandpass filter has been applied to both data sets. Time stamps in UTC are embedded in each panel. Comparing to Fig. 5 at 02:00 UTC, we recognize the prominent negative perturbation wave that is followed by a strong positive perturbation. There is good agreement between the simulation and observations in terms of amplitude, location and wavelength of this pattern. We see the waves propagating westward at later times and leaving the region of the TA. In the 06:00 UTC panel a positive perturbation located above the Oklahoma Panhandle precipitation system starts near 37°N at the western side of the TA region and then propagates southeastward. There is again good agreement in amplitudes and size of this feature between model and observations. At 12:00 UTC precipitation and wave activity have mostly calmed down, but pressure perturbations on the order of 30 Pa remain. The model predicts the spatial extent and magnitudes of these residual perturbations very well. Disagreement, particularly in the southeast, may be attributed to additional convection to the east of the domain that may generate waves which were not captured by the simulation.

To better see the realistic representation of the timing, speed and amplitudes of the waves in the model, Fig. 10 shows time series from the simulations (panel a) and TA data (panel b). The TA data have been de-meaned and bandpass filtered from 1-8 h and the model domain-mean pressure has been subtracted from the simulated data at each time. All lines are normalized such that 1° in longitude corresponds to a pressure perturbation of 300 Pa. There are several differences in the details of the waves but the overall agreement between model and observations for the most intense wave trains is good. Red colors mark regions where rain exceeds 1 mm/10 min. To point out some similarities: In the 30-31°N panel, both model and observations show westward propagating waves during the time interval ~4-12 UTC. In the 32-33°N panel, there are east- and westward propagating waves that originate from a region with precipitation around 6-8 UTC. Eastward propagating waves are triggered in both the 36-37°N and 37-38°N panels, and they dissipate after traveling for about the same amount of time and distance in both observed and modeled data. However, focusing on the red regions, which indicate precipitation, there is evidence from this comparison that perturbations may be underestimated in the model in regions where there was precipitation.

Figure 11 compares the simulated (solid histograms) and observed (dashed histograms) absolute perturbation pressure amplitudes of Fig. 10 close to convective regions (red) and to areas in the far-field (blue), defined here as regions that are separated by at least 0.75° of latitude/longitude from locations where rain rates greater than 1 mm/10 min are observed. Data are normalized by the total number of grid points in the far-field and grid points in the vicinity of convection, respectively. The relative occurrence frequency of large perturbation pressure amplitudes is much greater for regions in the vicinity of convection, even though substantial amplitudes greater than 200 Pa are reached in the observed far-field wave field. The potential for these waves to interact with or trigger remote convection will be discussed further in Section 4. Furthermore we see that the model underestimates the amplitudes of waves in regions where there was precipitation, which we label as convectively coupled waves. We hypothesize that this difference between model and observation is due to the fact that the model does not include moist processes, e.g. mesoscale updrafts and downdrafts, cold pools, and condensate mass. For instance, Bacmeister et al. (2012) show that the mass of condensate in convective clouds can significantly influence surface pressure, leading to corrections on the order of ∼100 Pa.

The vertical velocity field in Fig. 6 and the momentum flux spectrum at 17 km in Fig. 8 indicate that some of the wave energy also propagates upward into the stratosphere. The Atmospheric Infrared Sounder (AIRS) aboard NASA's Aqua satellite is a hyper-spectral imager, and can observe gravity wave signals in the stratosphere at 4.3 micron as well as cloud top brightness temperatures at 8.1 micron Hoffmann and Alexander (2010). Low 8.1 micron brightness temperatures observed by AIRS when the satellite passed over 36°N, 98°W at 08:05 UTC on June 29 indicate a mesoscale convective system with convection overshooting the tropopause (left panel of Fig. 12). This precipitation system is seen in the right panel of Fig. 2. Simultaneous 4.3 micron brightness temperature perturbations indicate stratospheric gravity waves propagating to the east from this location.

Eastward propagating waves were seen at the surface as well, see Fig. 5 at 10:00 UTC and the 35°N-36°N panel of Fig. 10. Fig. 13 is a zonal cross section at 07:00 UTC at 35.5°N, showing the simulated vertical velocity field in shades of gray and the heating/cooling region in purple. It shows the deep tropospheric waves that can be seen at the surface and waves propagating eastward into the stratosphere that are seen by the satellite.

4. Potential wave impacts on convection

In the previous sections we have seen that the model is capable of producing realistic gravity waves in the troposphere and above. Unlike surface or satellite observations the simulations contain information about the vertical structure of these waves and give us a more complete picture of their properties. In the case selected for this study, gravity waves triggered by one precipitation system encounter convection that is separated by several hundreds of kilometers. In this section we will examine whether the gravity waves may potentially play a role in strengthening the second precipitation system.

Fig. 14 displays hourly maps of vertical displacement at 850 hPa calculated as

$$\Delta z = -\Delta\theta \left(\frac{\partial\theta}{\partial z}\right)^{-1}, \tag{5}$$

where $\Delta\theta$ is the potential temperature perturbation at 850 hPa and $\partial\theta/\partial z$ is the vertical gradient of potential temperature, obtained from the initialization profile Fig. 4. Each panel shows the 2000 km $\times$ 2000 km WRF model domain, and time in UTC is given in the bottom left of each panel. Precipitating regions as determined by the radar observations are again marked in red. The blue box encloses the Oklahoma Panhandle precipitation system and numbers above each box show the accumulated hourly areal mean precipitation in mm for the area of the box. To better resolve the temporal evolution of precipitation inside the box the plot at the top of Fig. 14 shows the corresponding mean 10 min rain rates between 00:00 and 08:00 UTC.

We observe a westward propagating wave consisting of a wide-spread area with negative displacement followed by a well-defined positive-displacement. These waves are triggered by the precipitation system located in the center of the domain at 01:00 UTC and their signature was also apparent in the pressure perturbations shown in Fig. 5. An approximate doubling of the precipitation rate occurs as the positive phase of the propagating wave encounters the precipitation system active inside the box. This information is insufficient to establish a causal relationship between the wave and the strengthening of the precipitation system but it is consistent with the hypothesis that the gravity wave vertical displacements on the order of several hundred meters may alternately interfere with active convection and enhance it. There are many more factors that may influence the life cycle of this system, like changes in the background atmosphere that the idealized model cannot capture or the natural life cycle of the system.

Fig. 15 is a Hovmöller diagram of vertical displacement at 34°N showing the region 104.1°W to 94.4°W. The latitude of 34°N was chosen because it corresponds to the part of the circular wave train that is propagating to the west without much of a north- or southward component. This allows determination of the propagation speed when plotting against distance at a constant latitude. Precipitation is shown in red. The black dashed (dotted) lines mark constant propagation speeds of 40 (20) m/s relative to the mean zonal wind of 3 m/s in the heating region. We can see that the negative displacement pressure wave has a faster propagation speed than the positive displacement wave. The positive wave travels at a velocity close to the $n = 2$ mode, (see Table 1). The positive perturbation remains visible at the surface at distances far away from its origin, as opposed to the negative wave which appears to be more dispersive. This is consistent with the horizontal maps shown in Fig. 14. The discussion in the last paragraph of Section 2.c suggests further that the negative displacement wave would propagate upward more quickly than the positive wave owing to its larger horizontal phase speed, which is proportional to the ratio of the vertical group velocity to the horizontal group velocity (Eq. 1). This effect may contribute to the more rapid attenuation of the negative displacement signal at the surface.

The linear response to gravity waves from a radially symmetric heating profile on isentropic displacements near the surface has been calculated in Mapes (1993). They assumed a heating profile consisting of two modes, one with a vertical wavelength of twice the depth of the heating (n=1) and one with a wavelength equal to the depth of the heating (n=2). In agreement with our nonlinear simulations and the TA observations they report that 3 h after a heating pulse, low-level isentropes are lifted at a distance of about 250 km from the heating while the faster-propagating $n = 1$ results in subsidence at distance of about 500 km, see their Fig. 4b. The temporal and spatial scales seen here are consistent with the observational study by Lac et al. (2002), who found new convective cells appearing after a few hours and several hundred kilometers away from previous intense convection.

5. Summary

In this case study we simulated gravity waves generated by latent heating in precipitation systems over the central US. Model and observations show that these waves are associated with surface pressure signals that propagate distances longer than several hundred km and commonly exceed amplitudes of 100 Pa. In our model, described previously in Stephan and Alexander (2015), waves are forced by a temporally and spatially varying heating/cooling field that is derived directly from radar-observed precipitation. This approach permits a direct comparison to surface pressure variations measured by barometers in the USArray Transportable Array and we find that wave amplitudes agree well outside of regions where there was precipitation. The model renders the 3-dimensional far-field wave structure visible, which normally is unknown because measurements tend to be limited to the surface or provide vertical information at individual points only.

We analyzed wave propagation characteristics across the full vertical extent of the troposphere and found that linear theory can successfully predict the propagation speed of the simulated waves from the shape of the vertical heating profiles. From Fig. 8, slower waves with speeds < 5 m/s are relatively more prominent at the surface, and faster waves > 20 m/s are relatively more prominent near the tropopause, which can be understood as a consequence of their respective slow and fast vertical group velocities. Waves with intermediate speeds of 5-20 m/s are common at all levels. Similar wave signatures as those seen in the model were also observed in an overpass of the AIRS satellite instrument, indicating that waves measured at the surface and waves observed in the stratosphere are originating from common convective sources.

Vertical air parcel displacements at 850 hPa caused by waves propagating into regions that are far away from active convection exceed several hundred meters. In particular, we found evidence that the lifting phase of a 20 m/s propagating wave could be potentially responsible for an observed intensification of a separate developing precipitation system. The interaction of the propagating precipitation system with the convection occurred several hundred kilometers away from the origin of the wave and roughly 5 h after the wave was triggered. Our case study alone cannot provide enough evidence to prove that the intensification of precipitation is caused by the gravity wave, but it demonstrates that our method may be useful for future research. The modeling approach allows switching individual convective cells on or off, which can provide a clean way of disentangling coupled systems of waves and convection.

The approach, however, may not perform as well in other conditions. The case chosen for this study is particularly suitable for carrying out a comparison between simulated and observed waves because of well-defined, strong and isolated precipitation systems. Convection in the vicinity, but outside the model domain would generate additional waves that a simulation would miss and cause disagreement. Furthermore, the precipitation systems in this study developed within a region dominated by a broad ridge of high pressure. Relatively weak gradients in the horizontal profiles of pressure, wind and temperature may contribute to a successful comparison. It is possible that our method of initializing the model with a horizontally uniform environment is not suitable for synoptic situations with strong gradients.

Acknowledgments.

The authors would like to thank the three anonymous reviewers for their constructive comments to improve the manuscript. We would like to thank Dr. Stan Trier, Noah Brenowitz and Professor Brian Mapes for insightful discussions. This work was supported by grant number AGS–1318932 from the National Science Foundation programs in Physical and Dynamic Meteorology and Climate and Large-scale Dynamics and by NSF award EAR - 1358520. Data used in this study are Next-Generation Radar Level-III products available from the National Oceanic and Atmospheric Administration Satellite and Information Service (http://www.ncdc.noaa.gov/data-access/radar-data), the Modern-Era Retrospective analysis for Research and Applications (MERRA) reanalysis (http://gmao.gsfc.nasa.gov/research/merra/), data from the USArray (http:// www.usarray.org/researchers/data) and AIRS data distributed by the NASA GES DISC. The Weather Research and Forecasting model (http://wrf-model.org/index.php) is supported by the National Center for Atmospheric Research.

REFERENCES

Alexander, M. J. and J. R. Holton, 2004: On the spectrum of vertically propagating gravity waves generated by a transient heat source. *Atmos. Chem. Phys.*, **4**, 923–932, [Available online at `www.atmos-chem-phys.org/acp/4/923/`].

Bacmeister, J. T., P. H. Lauritzen, A. Dai, and J. E. Truesdale, 2012: Assessing possible dynamical effects of condensate in high resolution climate simulations. *Geophys. Res. Lett.*, **39**, L04806, doi:10.1029/2011GL050533.

Busby, R., F. Vernon, R. Newman, and L. Astiz, 2006: Eos Trans. AGU 87 (52). Fall Meet. Suppl., Abstract U41B-0820. Earth-Scopes USArray: Advancing eastward.

De Groot-Hedlin, C., M. Hedlin, and K. Walker, 2014: Detection of gravity waves across the USArray: A case study. *Earth and Planetary Sci. Lett.*, **402**, 346–352, doi:10.1016/j.epsl.2013.06.042.

Fovell, R. G., 2002: Upstream influence of numerically simulated squall-line storms. *Q. J. R. Meteorol. Soc.*, **128**, 893–912.

Fritts, D. C. and M. J. Alexander, 2003: Gravity wave dynamics and effects in the middle atmosphere. *Rev. Geophys.*, **41**, 1003, doi:10.1029/2001RG000106.

Hoffmann, L. and M. J. Alexander, 2010: Occurrence frequency of convective gravity waves during the North American thunderstorm season. *J. Geophys. Res.*, **115**, doi:10.1029/2010JD014401.

Koch, S. E. and L. M. Siedlarz, 1999: Mesoscale gravity waves and their environment in the central United States during STORM-FEST. *Mon. Wea. Rev.*, **127 (12)**, 2854–2879, doi:10.1175/1520-0493(1999)127⟨2854:MGWATE⟩2.0.CO;2.

Koppel, L. L., L. F. Bosart, and D. Keyser, 2000: A 25-yr climatology of large-amplitude hourly surface pressure changes over the conterminous United States. *Monthly Weather Review*, **128 (1)**, 51–68, doi:10.1175/1520-0493(2000)128⟨0051:AYCOLA⟩2.0.CO;2.

Lac, C., J.-P. Lafore, and J.-L. Redelsperger, 2002: Role of gravity waves in triggering deep convection during TOGA COARE. *J. Atmos. Sci.*, **59 (8)**, 1293–1316, doi:10.1175/1520-0469(2002)059⟨1293:ROGWIT⟩2.0.CO;2.

Lane, T. P. and F. Zhang, 2011: Coupling between gravity waves and tropical convection at mesoscales. *J. Atmos. Sci.*, **68 (11)**, 2582–2598, doi:10.1175/2011JAS3577.1.

Mapes, B. E., 1993: Gregarious tropical convection. *J. Atmos. Sci.*, **50**, 2026–2037.

Nicholls, M. E., R. A. Pielke, and W. R. Cotton, 1991: Thermally forced gravity waves in an atmosphere at rest. *J. Atmos. Sci.*, **48**, 1869–1884, doi:http://dx.doi.org/10.1175/1520-0469(1991)048⟨1869:TFGWIA⟩2.0.CO;2.

OFCM, 2006: Federal meteorological handbook No. 11 part c. OFCM Tech. Rep. FCM-H11C-2006.

Pandya, R. E. and M. J. Alexander, 1999: Linear stratospheric gravity waves above convective thermal forcing. *J. Atmos. Sci.*, **56**, 2434–2446.

Rienecker, M. M., et al., 2011: MERRA: NASA's Modern-Era Retrospective Analysis for Research and Applications. *J. Climate*, **24**, 3624–3648, doi:10.1175/JCLI-D-11-00015.1.

Ruppert, J. H. and L. F. Bosart, 2014: A case study of the interaction of a mesoscale gravity wave with a mesoscale convective system. *Monthly Weather Review*, **142 (4)**, 1403–1429, doi:10.1175/MWR-D-13-00274.1.

Shige, S. and T. Satomura, 2001: Westward generation of eastward-moving tropical convective bands in TOGA COARE. *J. Atmos. Sci.*, **58**, 3724–3740, doi:http://dx.doi.org/10.1175/1520-0469(2001)058⟨3724:WGOEMT⟩2.0.CO;2.

Skamarock, W., J. B. Klemp, J. Dudhia, et al., 2008: A description of the Advanced Research WRF Version 3. NCAR Technical Note NCAR/TN-475+STR. doi:10.5065/D68S4MVH.

Song, I.-S., H.-Y. Chun, and T. P. Lane, 2003: Generation mechanisms of convectively forced internal gravity waves and their propagation to the stratosphere. *J. Atmos. Sci.*, **60 (16)**, 1960–1980, doi:10.1175/1520-0469(2003)060⟨1960:GMOCFI⟩2.0.CO;2.

Stechmann, S. N. and A. J. Majda, 2009: Gravity waves in shear and implications for organized convection. *J. Atmos. Sci.*, **66 (9)**, 2579–2599, doi:10.1175/2009JAS2976.1.

Stephan, C. C. and M. J. Alexander, 2014: Summer season squall line simulations: Sensitivity of gravity waves to physics parameterization and implications for their parameterization in global climate models. *J. Atmos. Sci.*, **71**, 3376–3391, doi:10.1175/JAS-D-13-0380.1.

Stephan, C. C. and M. J. Alexander, 2015: Realistic simulations of atmospheric gravity waves over the Continental U.S. using precipitation radar data. *J. Adv. Model. Earth Syst.*, **07**, 823–835, doi:10.1002/2014MS000396.

Tulich, S. N. and B. E. Mapes, 2008: Multiscale convective wave disturbances in the tropics: Insights from a two-dimensional cloud-resolving model. *J. Atmos. Sci.*, **65 (1)**, 140–155, doi:10.1175/2007JAS2353.1.

Tulich, S. N., D. A. Randall, and B. E. Mapes, 2007: Vertical-mode and cloud decomposition of large-scale convectively coupled gravity waves in a two-dimensional cloud-resolving model. *J. Atmos. Sci.*, **64**, 1210–1229, doi:10.1175/JAS3884.1.

Yang, M.-J. and R. A. Houze, 1995: Multicell squall-line structure as a manifestation of vertically trapped gravity waves. *Mon. Wea. Rev.*, **123**, 641–660, doi:10.1175/1520-0493(1995)123⟨0641:MSLSAA⟩2.0.CO;2.

List of Tables

1 Theoretical phase speeds c, from Eq. (3), and percentage of explained variance, for the first ten Fourier modes. Please refer to the text for further explanation. 23

TABLE 1. Theoretical phase speeds c, from Eq. (3), and percentage of explained variance, for the first ten Fourier modes. Please refer to the text for further explanation.

n	c $[m/s]$	Expl. Var. [%]
1	42.6	61.0
2	21.3	18.8
3	14.2	13.1
4	10.6	2.8
5	8.5	2.4
6	7.1	0.7
7	6.1	0.6
8	5.3	0.2
9	4.7	< 0.1
10	4.3	< 0.1

List of Figures

1 Deployment history of operating Transportable Array stations equipped with MEMS (Micro Electro-Mechanical System) pressure sensors for the years 2010-2013. 28

2 Mosaics of radar reflectivity generated with NEXRAD data obtained from the Iowa State Environmental Mesonet Archive https://mesonet.agron.iastate.edu. Courtesy of Dave Ahijevych. 29

3 Model domain measuring 2000 km × 2000 km (gold) and the 37 NEXRAD radar stations that are used for deriving a 4 km × 4 km 10 min precipitation mosaic. The four-letter identification code indicates the location and the circles the 230 km radius of individual stations. The simulation is initialized using MERRA vertical profiles averaged inside the dashed black box. 30

4 Initialization profiles of potential temperature and horizontal winds computed from 24-h mean MERRA profiles. MERRA grid points inside the black dashed box shown in Fig. 3 were averaged. 31

5 Maps of simulated perturbation pressure, defined as the deviation from the domain mean pressure at each time, at 500 m altitude. Red areas mark regions that exceed the convective threshold of 1 mm/10 min, i.e. regions where a heating/cooling field is turned on in the simulation. 32

6 Zonal cross sections of vertical velocities (top) and perturbation pressure (bottom) at 34°N and 00:40 UTC to the west of active convection. The origin of the x-axis is located at 96.2°W. The color scale for the top panel is saturated at ± 1.5 m/s to emphasize the far-field waves, but vertical velocity values close to the heat source range from -2.3 m/s to +3.0 m/s. The shape of the mean heating/cooling profile inside the convective region is shown to the left of each panel. 33

7 Decomposition of the heating profile associated with the 99th percentile rain rate. The full heating profile is shown in the right panel (thick black line). The sums of the first 10 (left panel) and first 3 (middle panel) Fourier components are colored lines. For details on the computation, please refer to the text. 34

8 Normalized absolute momentum flux spectra at 3 km (left panel) and 17 km (right panel) as a function of horizontal wavenumber and frequency. A three-dimensional Fourier analysis was applied to obtain each spectrum as a function of frequency, zonal wavenumber k, and meridional wavenumber l. The horizontal wavenumber, shown on the x-axis, is given by $\sqrt{(k^2 + l^2)}$ and is independent of the direction of wave propagation. Lines of constant phase speed in units of m/s are shown in white. 35

9 Model perturbation pressure in units of Pa sampled at locations of TA installations and the corresponding TA recorded observations at 2-h intervals. A 1-8 h bandpass filter has been applied to both data sets. Time in UTC is shown at the bottom inside each panel. 36

10 Times series of model predictions and recorded data at locations of stations in the TA. We have arranged all model predictions in a set of 8 sections in a), with observations in b). Each panel contains recordings (or model predictions) from all stations that were located in a narrow east-west corridor - with the latitude limits given in the figure captions, and with the zero-anomaly location of each trace along the x-axis being determined by the stations longitude. Amplitudes are normalized such that 300 Pa correspond to 1° of longitude. The observed time series were bandpass filtered from 1-8 h. For simulated data the domain-mean pressure at each time has been removed. Regions of active convection are marked in red (rain rates exceeding a threshold of 1 mm/10 min). 37

11 Simulated absolute perturbation pressure amplitudes in the vicinity of precipitating regions (red), defined as areas separated by less than 0.75° of latitude/longitude from locations where rain rates greater than 1 mm/10 min are observed and far-field areas (blue). Simulated data are shown as solid histograms and observed data as dashed histograms. All data are normalized by the total number of grid points that lie in the far-field and in the vicinity of convection, respectively. 38

12 8.1 micron brightness temperatures (left) and 4.3 micron brightness temperature perturbations (right) observed by AIRS at 08:05 UTC on June 29 indicate a mesoscale convective system with convection overshooting the tropopause and eastward propagating gravity waves, respectively. The images are computed using the method described in Hoffmann and Alexander (2010). 39

13 Zonal cross section at 07:00 UTC at 35.5°N, showing simulated vertical velocities (shades of gray) and the heating/cooling region (purple) at contour intervals of 0.003 K/s. 40

14 Hourly maps of vertical displacement at 850 hPa computed from simulated potential temperature perturbations. Time in hours UTC is indicated in the bottom left of each panel. Red areas mark active convection (rain rates exceeding 1 mm/10 min for some time during the hour). The areal-mean precipitation rate in mm/hour inside the small blue box in each panel is shown above the box. The graph at the top of the figure shows the temporal evolution of areal-mean 10 min precipitation inside this small blue box between 00:00 and 08:00 UTC. 41

15 Hovmöller diagram of 850 hPa vertical displacement at 34°N showing the region 104.1°W to 94.4°W. Black dashed (dotted) lines mark constant propagation speeds of 40 (20) m/s relative to the mean zonal wind of 3 m/s in the heating region. Precipitating regions are shown in red (rain rates exceeding 1 mm/10 min). 42

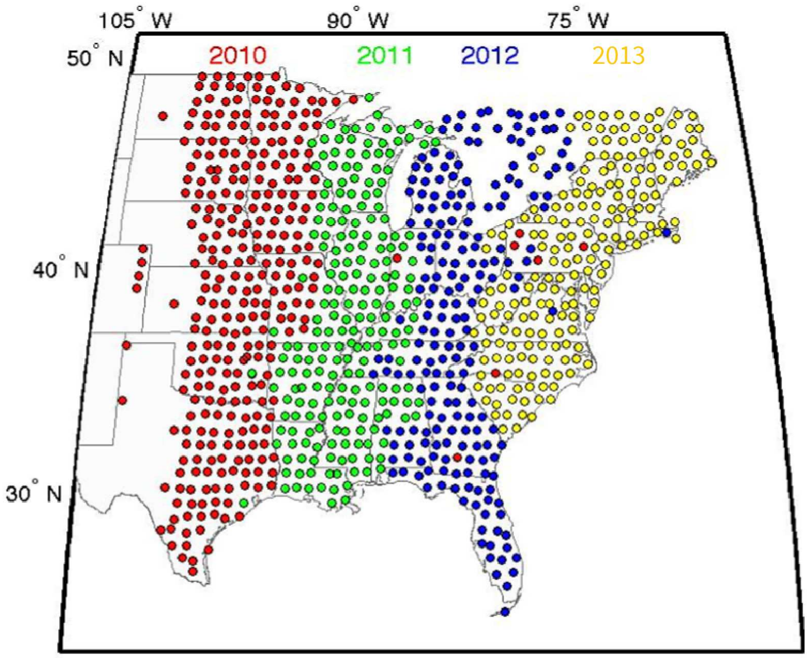

Fig. 1. Deployment history of operating Transportable Array stations equipped with MEMS (Micro Electro-Mechanical System) pressure sensors for the years 2010-2013.

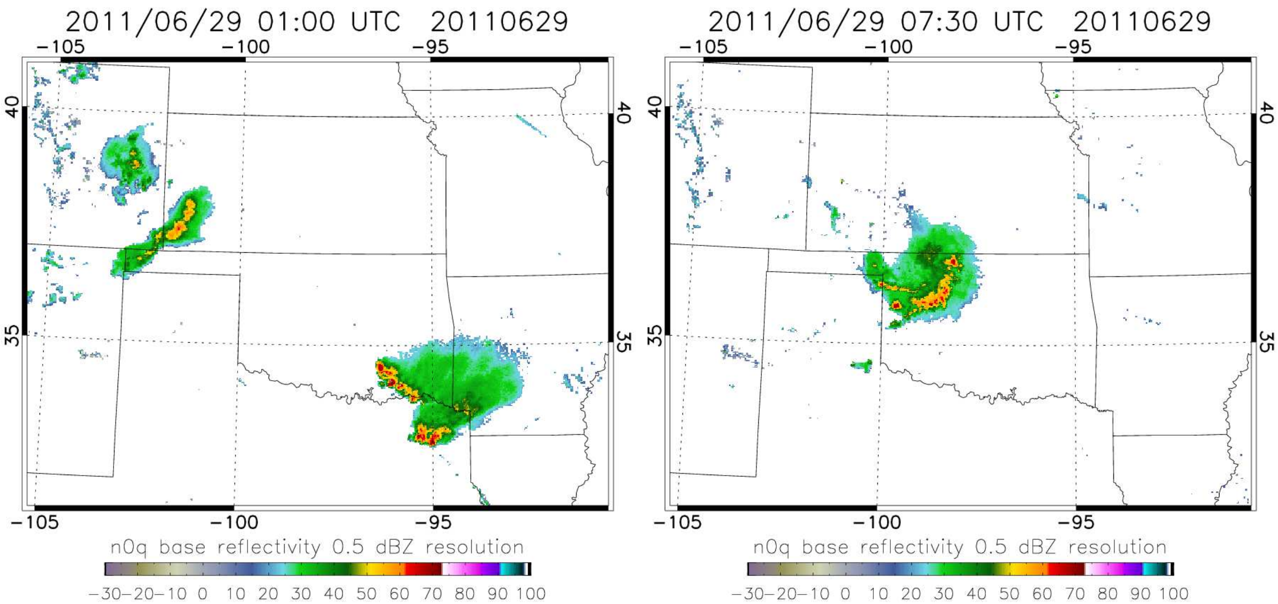

Fig. 2. Mosaics of radar reflectivity generated with NEXRAD data obtained from the Iowa State Environmental Mesonet Archive https://mesonet.agron.iastate.edu. Courtesy of Dave Ahijevych.

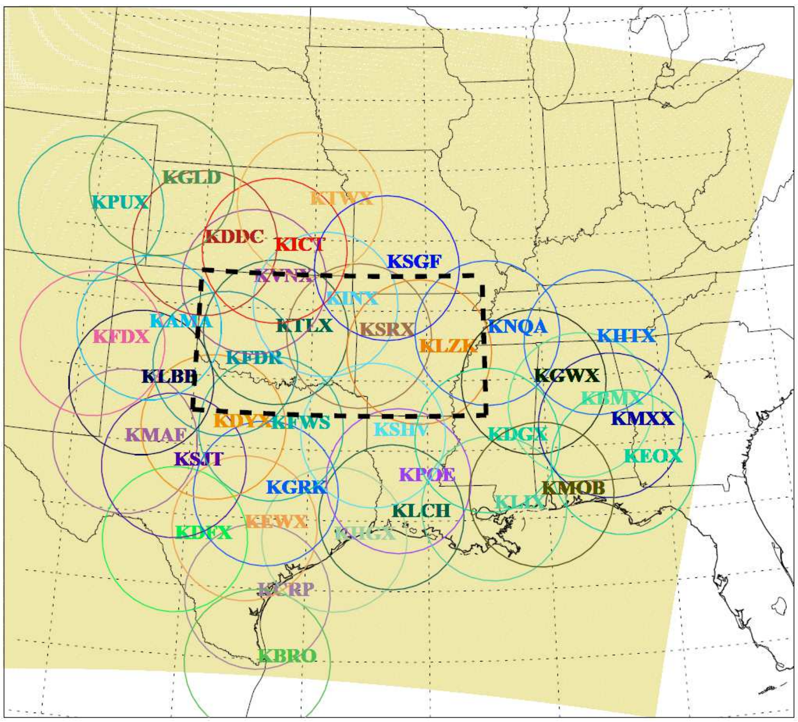

FIG. 3. Model domain measuring 2000 km $\times$ 2000 km (gold) and the 37 NEXRAD radar stations that are used for deriving a 4 km $\times$ 4 km 10 min precipitation mosaic. The four-letter identification code indicates the location and the circles the 230 km radius of individual stations. The simulation is initialized using MERRA vertical profiles averaged inside the dashed black box.

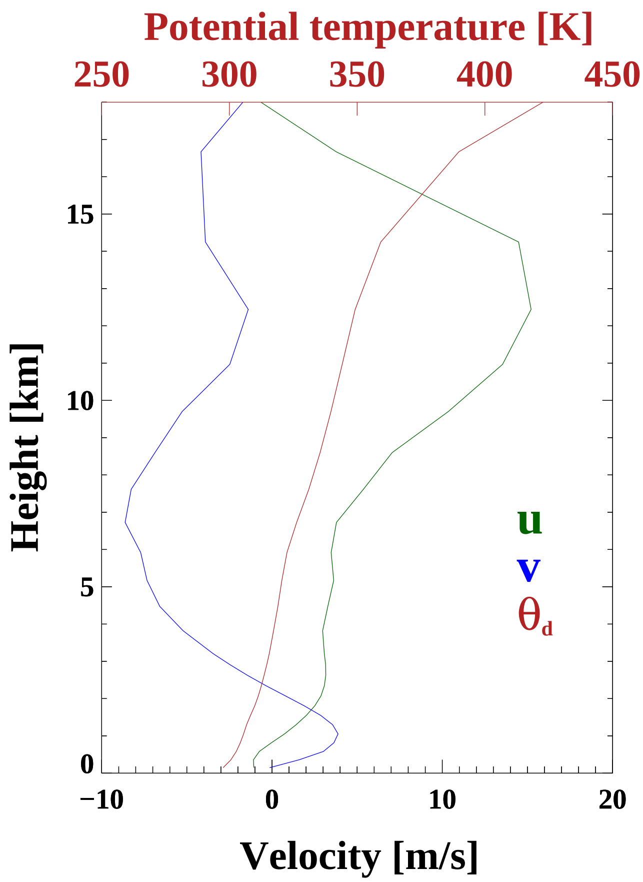

FIG. 4. Initialization profiles of potential temperature and horizontal winds computed from 24-h mean MERRA profiles. MERRA grid points inside the black dashed box shown in Fig. 3 were averaged.

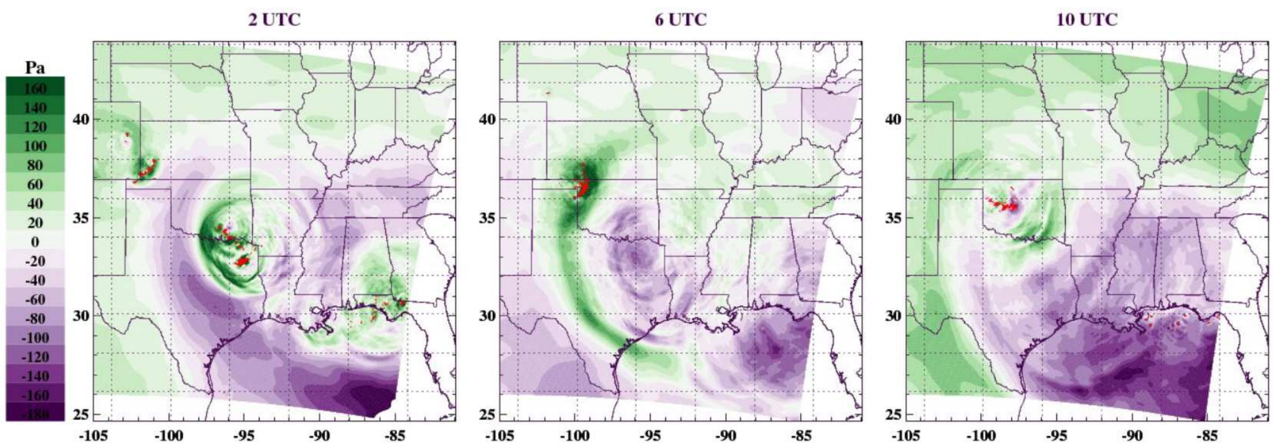

Fig. 5. Maps of simulated perturbation pressure, defined as the deviation from the domain mean pressure at each time, at 500 m altitude. Red areas mark regions that exceed the convective threshold of 1 mm/10 min, i.e. regions where a heating/cooling field is turned on in the simulation.

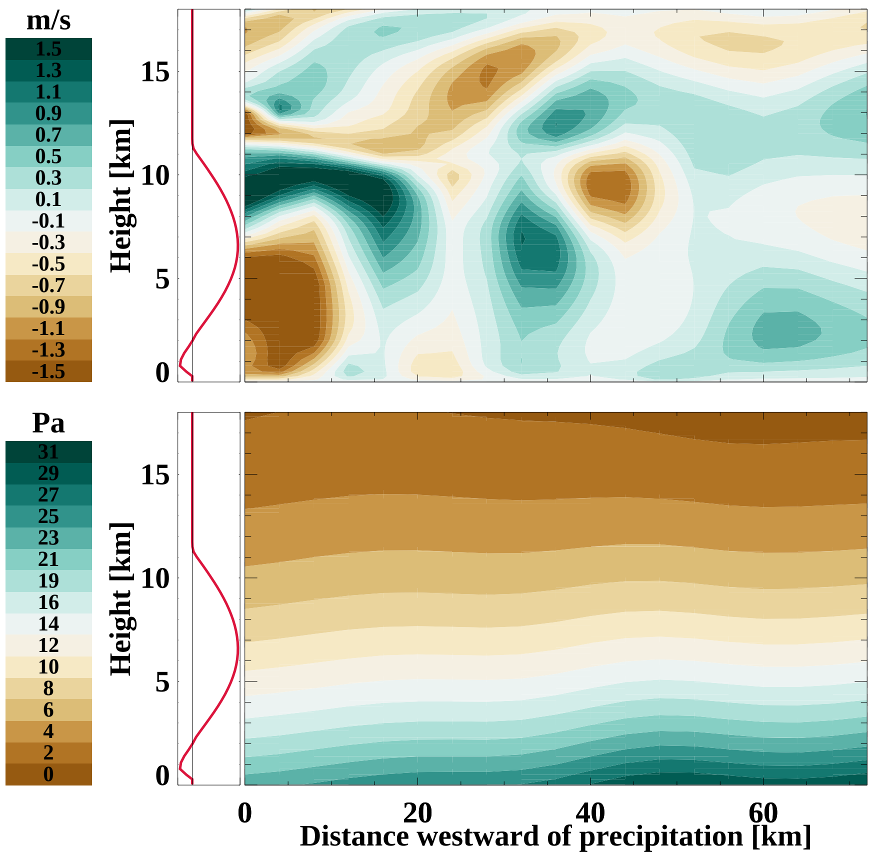

FIG. 6. Zonal cross sections of vertical velocities (top) and perturbation pressure (bottom) at 34°N and 00:40 UTC to the west of active convection. The origin of the x-axis is located at 96.2°W. The color scale for the top panel is saturated at ± 1.5 m/s to emphasize the far-field waves, but vertical velocity values close to the heat source range from -2.3 m/s to +3.0 m/s. The shape of the mean heating/cooling profile inside the convective region is shown to the left of each panel.

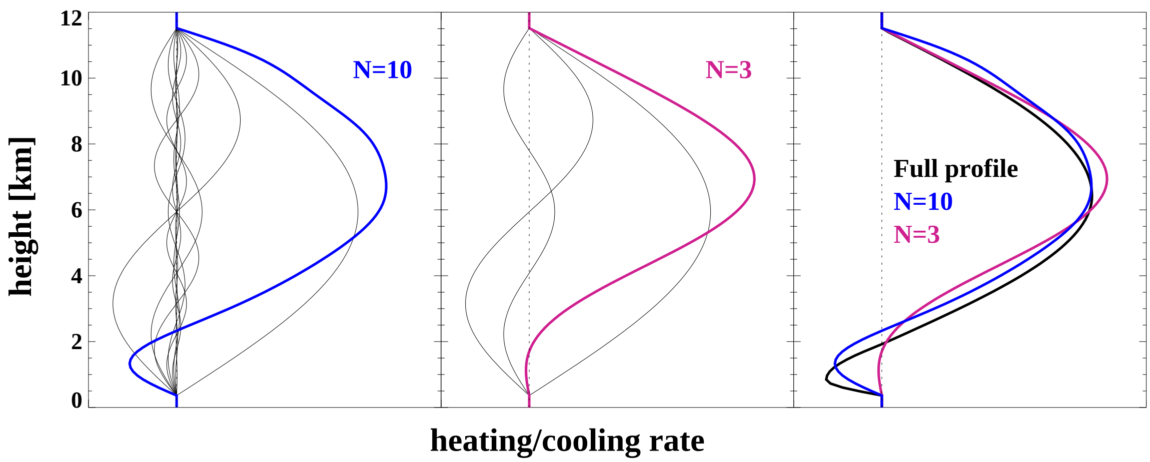

FIG. 7. Decomposition of the heating profile associated with the 99th percentile rain rate. The full heating profile is shown in the right panel (thick black line). The sums of the first 10 (left panel) and first 3 (middle panel) Fourier components are colored lines. For details on the computation, please refer to the text.

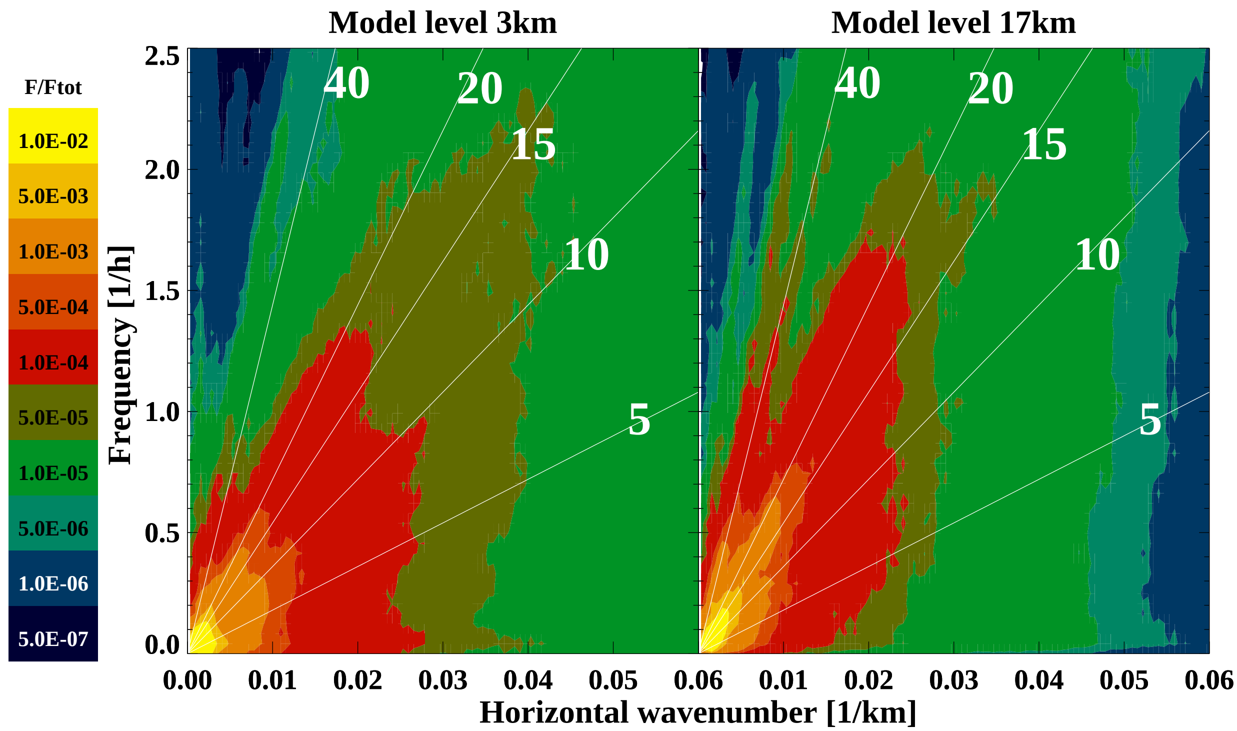

FIG. 8. Normalized absolute momentum flux spectra at 3 km (left panel) and 17 km (right panel) as a function of horizontal wavenumber and frequency. A three-dimensional Fourier analysis was applied to obtain each spectrum as a function of frequency, zonal wavenumber k, and meridional wavenumber l. The horizontal wavenumber, shown on the x-axis, is given by $\sqrt{(k^2 + l^2)}$ and is independent of the direction of wave propagation. Lines of constant phase speed in units of m/s are shown in white.

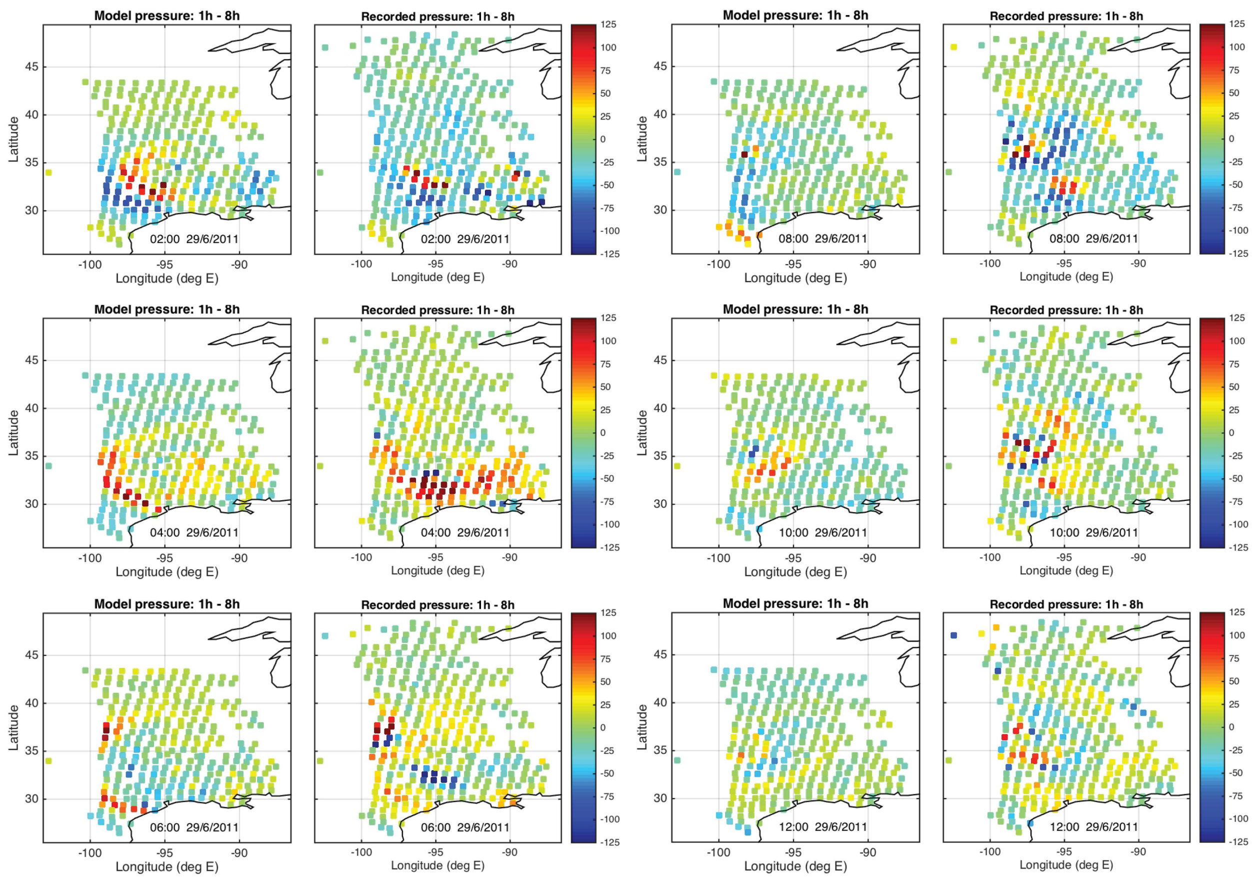

FIG. 9. Model perturbation pressure in units of Pa sampled at locations of TA installations and the corresponding TA recorded observations at 2-h intervals. A 1-8 h bandpass filter has been applied to both data sets. Time in UTC is shown at the bottom inside each panel.

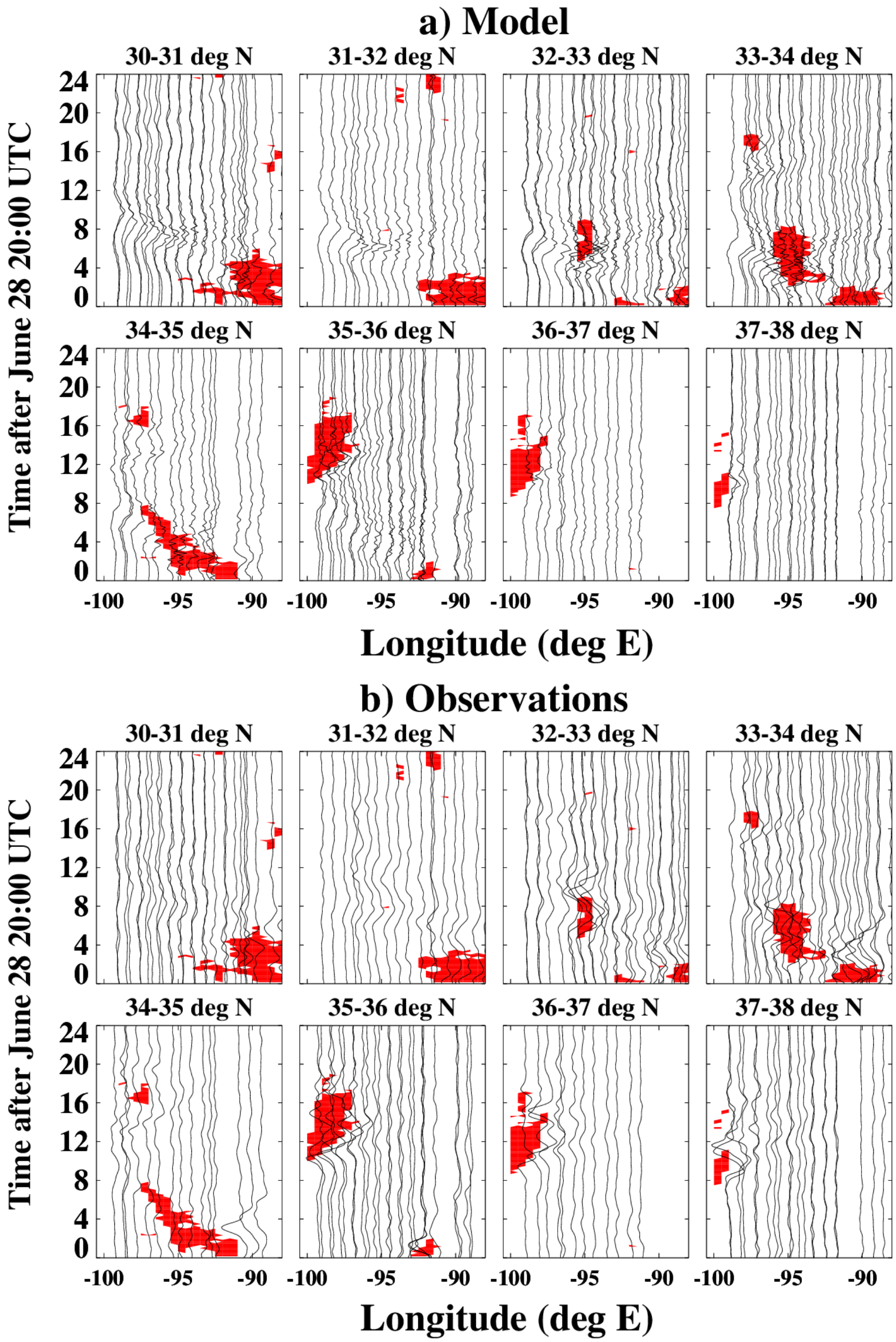

FIG. 10. Times series of model predictions and recorded data at locations of stations in the TA. We have arranged all model predictions in a set of 8 sections in a), with observations in b). Each panel contains recordings (or model predictions) from all stations that were located in a narrow east-west corridor - with the latitude limits given in the figure captions, and with the zero-anomaly location of each trace along the x-axis being determined by the stations longitude. Amplitudes are normalized such that 300 Pa correspond to 1° of longitude. The observed time series were bandpass filtered from 1-8 h. For simulated data the domain-mean pressure at each time has been removed. Regions of active convection are marked in red (rain rates exceeding a threshold of 1 mm/10 min).

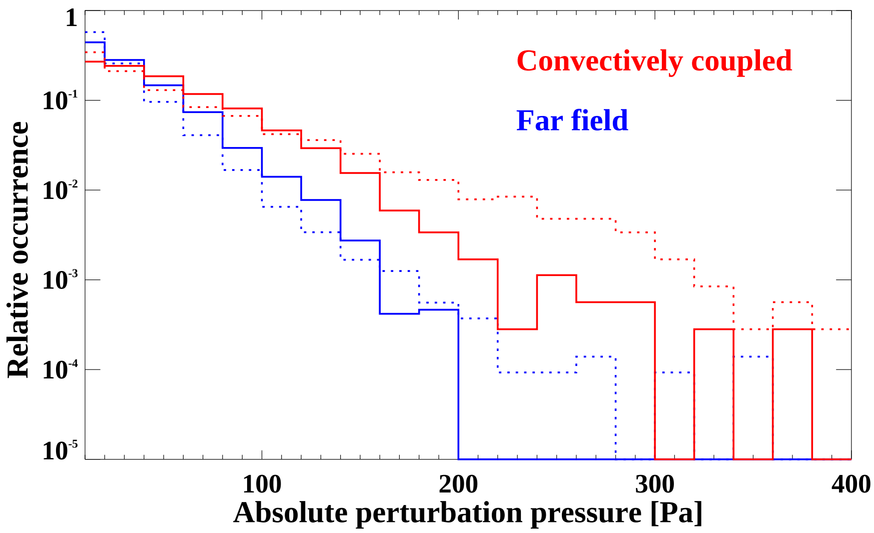

FIG. 11. Simulated absolute perturbation pressure amplitudes in the vicinity of precipitating regions (red), defined as areas separated by less than 0.75° of latitude/longitude from locations where rain rates greater than 1 mm/10 min are observed and far-field areas (blue). Simulated data are shown as solid histograms and observed data as dashed histograms. All data are normalized by the total number of grid points that lie in the far-field and in the vicinity of convection, respectively.

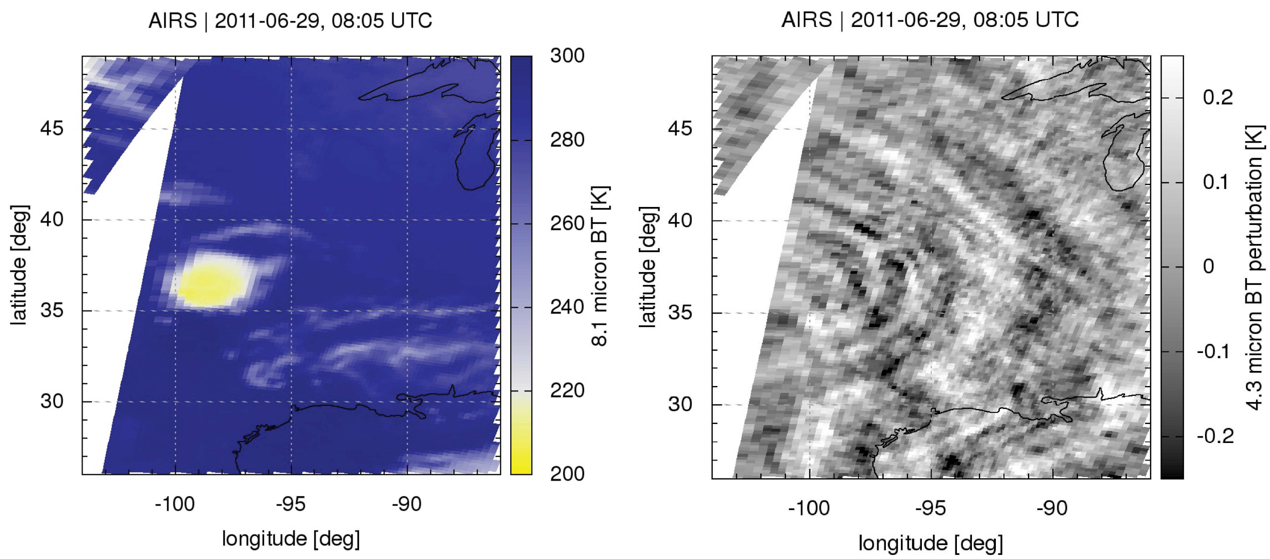

FIG. 12. 8.1 micron brightness temperatures (left) and 4.3 micron brightness temperature perturbations (right) observed by AIRS at 08:05 UTC on June 29 indicate a mesoscale convective system with convection overshooting the tropopause and eastward propagating gravity waves, respectively. The images are computed using the method described in Hoffmann and Alexander (2010).

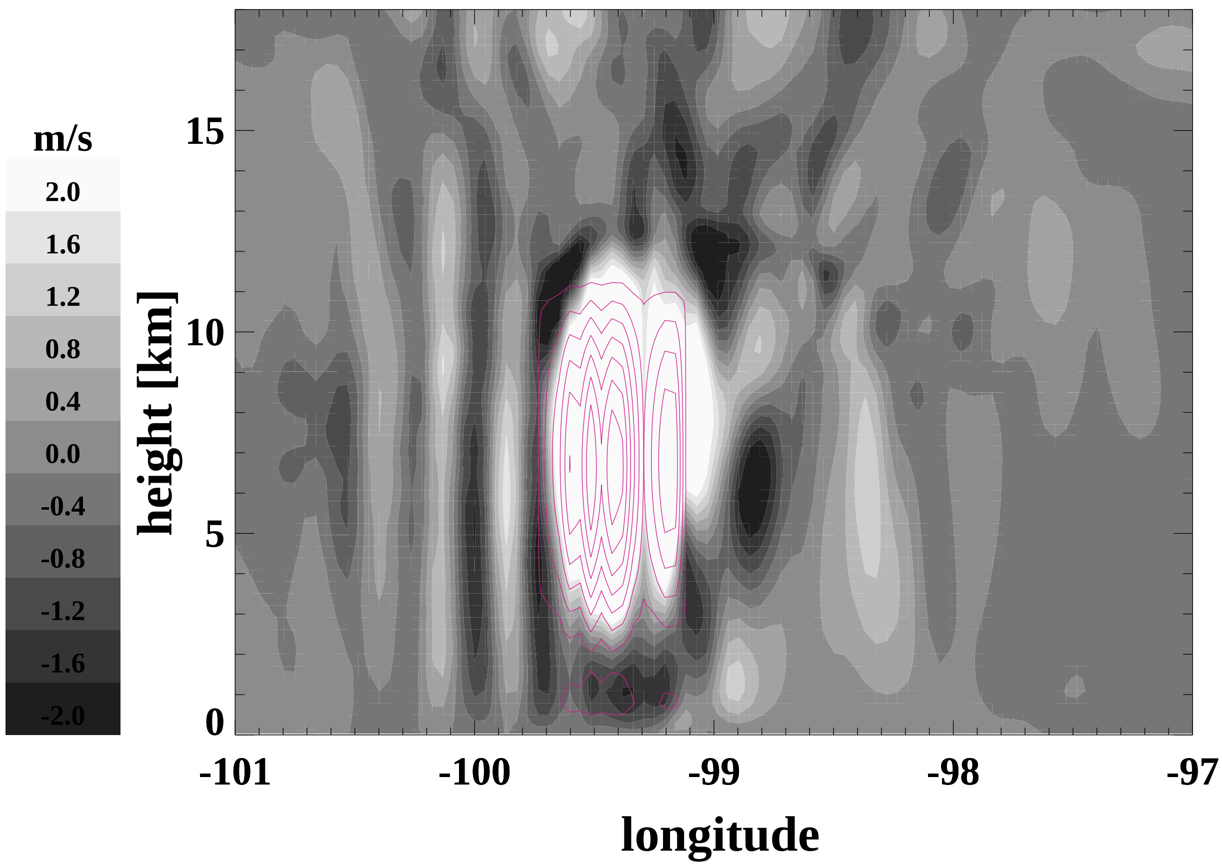

FIG. 13. Zonal cross section at 07:00 UTC at 35.5°N, showing simulated vertical velocities (shades of gray) and the heating/cooling region (purple) at contour intervals of 0.003 K/s.

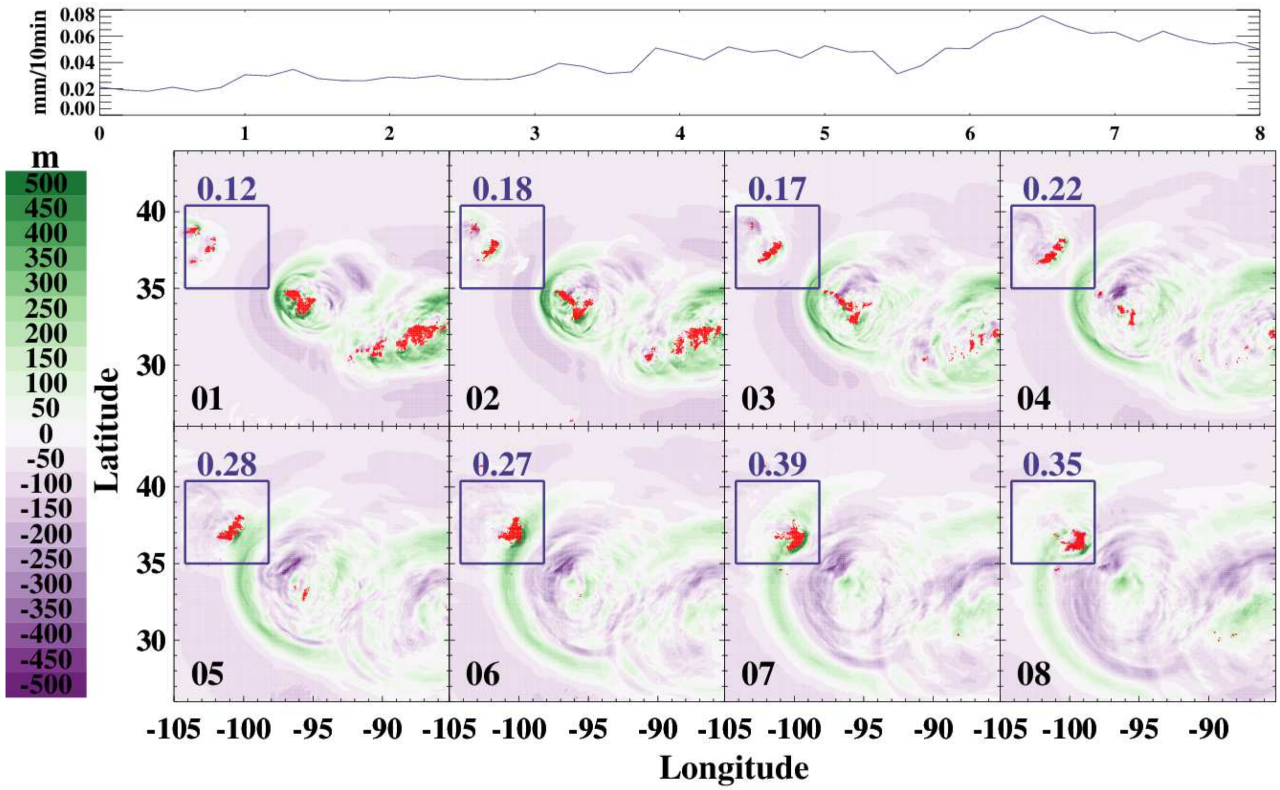

FIG. 14. Hourly maps of vertical displacement at 850 hPa computed from simulated potential temperature perturbations. Time in hours UTC is indicated in the bottom left of each panel. Red areas mark active convection (rain rates exceeding 1 mm/10 min for some time during the hour). The areal-mean precipitation rate in mm/hour inside the small blue box in each panel is shown above the box. The graph at the top of the figure shows the temporal evolution of areal-mean 10 min precipitation inside this small blue box between 00:00 and 08:00 UTC.

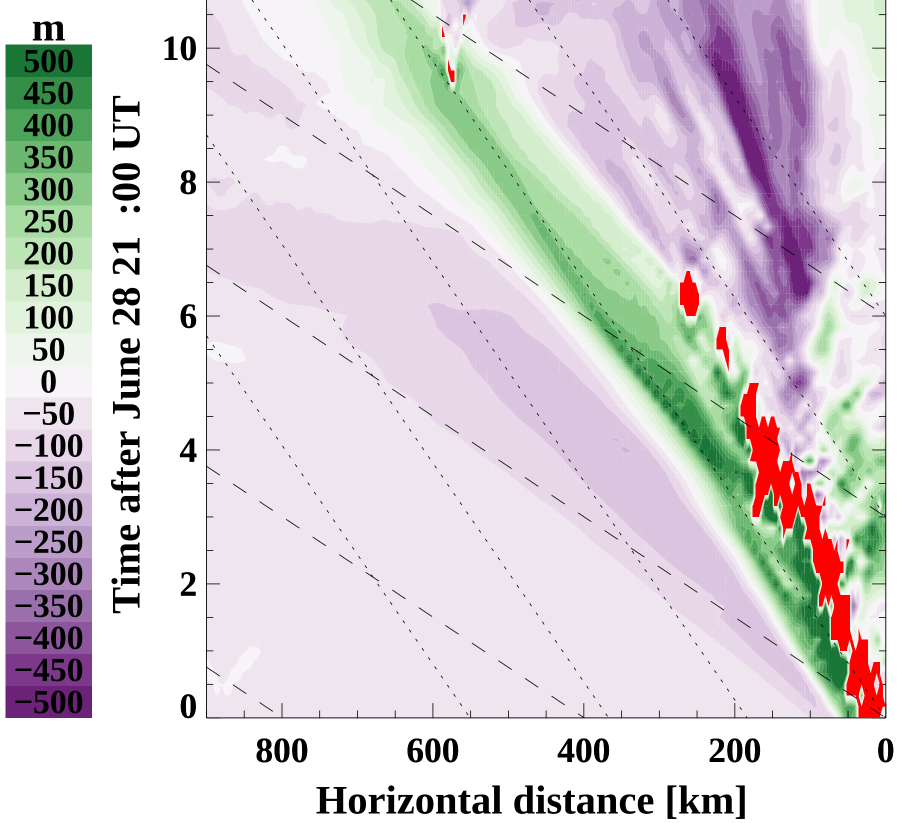

Fig. 15. Hovmöller diagram of 850 hPa vertical displacement at 34°N showing the region 104.1°W to 94.4°W. Black dashed (dotted) lines mark constant propagation speeds of 40 (20) m/s relative to the mean zonal wind of 3 m/s in the heating region. Precipitating regions are shown in red (rain rates exceeding 1 mm/10 min).